A parametric study of the source rate for outer radiation belt electrons using a Kalman filter

Q. Schiller,[1,2] X. Li,[1,2] J. Koller,[3] H. Godinez,[3] and D. L. Turner[4]

Received 31 March 2012; revised 9 July 2012; accepted 28 July 2012; published 13 September 2012.

[1] Data assimilation methods have become increasingly popular to describe the outer radiation belt energetic electron environment. We use a Kalman filter with inputs of 1) electron phase space density (PSD) for constant first and second adiabatic invariants, μ = 2083[MeV/G] and K = 0.03[$G^{1/2}R_E$] respectively, from a five satellite data set (three LANL-GEO, one GPS, and Polar), and 2) a one-dimensional radial diffusion model with loss and source terms included. We augment the Kalman filter to include the intensity of local acceleration in the state vector. The output is an estimate of PSD for the radial range of the outer radiation belt and the time-dependent amplitude parameter of a Gaussian shaped source rate term for given location and width. To further constrain the source rate parameters, a root mean square (RMS) analysis of the observation residual vector (a.k.a. innovation vector) is performed in a parameter space of source location and width. We analyze five storm periods spanning from July 30th to October 24th of 2002, and each period's unique solution in the location-width parameter space is assimilated with the Kalman filter for a continuous reanalysis of the full 87 day period. The source amplitude parameter is analyzed for insight into time periods of enhanced local heating, suppressed loss, or, as the parameter can take negative values, additional loss. The source is found to peak in the recovery phases of the storms where the rate is sufficient to repopulate the radiation belt in approximately one day, suggesting that local heating is a major contributor to the electron radiation belts during the recovery phase.

Citation: Schiller, Q., X. Li, J. Koller, H. Godinez, and D. L. Turner (2012), A parametric study of the source rate for outer radiation belt electrons using a Kalman filter, *J. Geophys. Res.*, *117*, A09211, doi:10.1029/2012JA017779.

1. Introduction

1.1. Understanding the Electron Radiation Belt

[2] The electron radiation belt, or outer Van Allen belt, is a toroidal region in space populated by relativistic electrons. These particles are trapped in the Earth's magnetosphere, but are constrained to 3 $\sim$ 7 Earth radii (R_E) and often have peaks in intensity between 4 and 5 R_E. The outer radiation belt is separated from the inner radiation belt, which consists of mostly energetic protons populating approximately 1.2 to 2.5 R_E, by a region of space generally empty of energetic particles called the slot region.

[3] The highly energetic electron environment in Earth's magnetosphere poses an incessant risk to spacecraft and organic tissue alike [*Baker*, 2001]. Furthermore, the particles overlap an array of commonly used spacecraft orbits, such as low-Earth, Global Positioning System (GPS), and geosynchronous (GEO). Understanding the physical processes in this environment is not only a scientific challenge but also critical to mitigate the risk to spacecraft and astronauts.

[4] The energetic electron environment changes continuously by various complex and not well-understood processes, such as localized heating (source), loss, and radial transport [e.g., *Li and Temerin*, 2001]. For example, whistler mode chorus waves, associated with increased geomagnetic and substorm activity, are believed to be a major contributor in locally accelerating 100 keV electrons to MeV energies [e.g., *Horne et al.*, 2007]. Recently, numerous studies have been published on modeling the waves' effects on the radiation belts [e.g., *Shprits et al.*, 2006; *Summers et al.*, 2007]. The source location has been characterized [*Meredith et al.*, 2002, 2003a, 2003b; *Santolík et al.*, 2005, 2009; *Li et al.*, 2009] to occur preferentially from approximately 4 < L < 6, but can occur from 3 < L < 10 [*Li et al.*, 2009].

[5] However, each individual process is difficult to quantify and understand its net contribution to the state of the system. *Reeves et al.* [2003] showed that geomagnetic storms can affect the delicate balance of these processes, resulting in a net increase or decrease of radiation belt electron fluxes, or sometimes no change at all, if comparing the post-storm level

[1]Laboratory for Atmospheric and Space Physics, University of Colorado, Boulder, Colorado, USA.
[2]State Key Laboratory of Space Weather, Chinese Academy of Sciences, Beijing, China.
[3]Los Alamos National Laboratory, Los Alamos, New Mexico, USA.
[4]Institute of Geophysics and Planetary Physics, University of California, Los Angeles, California, USA.

Corresponding author: Q. Schiller, Laboratory for Atmospheric and Space Physics, University of Colorado, 1234 Innovation Dr., Boulder, CO 80303, USA. (quintin.schiller@colorado.edu)

©2012. American Geophysical Union. All Rights Reserved.
0148-0227/12/2012JA017779

with the pre-storm level. Further complication of the problem lies in the restricted, single-point in situ measurements of spacecraft. These measurements have limited spatial and temporal coverage, often with large uncertainties. To address these challenges, the radiation belt community has turned to data assimilation to attempt to fill in the data gaps in space and time.

1.2. Data Assimilation and Recent Applications to Radiation Belts

[6] Data assimilation are methodologies that approximate, as accurately as possible, the true state of a system. They do so by blending observations with dynamical models of the system to optimally combine all available information. Data assimilation has been used extensively where sparse data is typical, such as applications in terrestrial weather [*Kalnay*, 2003], satellite orbit determination [*Tapley et al.*, 2004], unmanned aerial vehicle control [*Stachura and Frew*, 2011], and oceanography [*Evensen*, 1994]. The sparse and restricted measurements of the energetic electron environment make data assimilation a natural approach for us to form a global picture of the radiation environment around Earth.

[7] Data assimilation is a proven method to reconstruct aspects of the energetic electron environment in the outer radiation belt. One method, known as direct insertion, runs a physics-based model while substituting the in situ observations as they become available. The model then propagates the measurements into regions of interest that lack observations. Work by *Maget et al.* [2007] and *Bourdarie et al.* [2005, 2009] used the Salammbô code, developed at the Office National d'Etudes et de Recherche Aérospatiales in Toulouse, France [*Beutier and Boscher*, 1995], to directly insert PSD data in a 3D radiation belt model (see section 2.2 for discussion on radiation belt modeling). A 3D model more accurately describes the physical dynamics of the environment, but introduces additional challenges, such as requiring conjunctions between satellites to determine pitch angle distributions. On storm timescales, this limitation hinders the 3D code from reproducing the full dynamics of the environment and thus, 1D diffusion is a reasonable approach despite the inherent limitations in describing system dynamics.

[8] Another method of data assimilation is the Kalman filter [*Kalman*, 1960]. An early study by *Naehr and Toffoletto* [2005] showed that, for a simple one dimensional radial diffusion model, an extended Kalman filter (EKF) [*Jazwinski*, 1970] outperforms direct insertion for a highly idealized case. Furthermore, using an identical twin experiment (a method of assimilating a synthesized radiation belt environment to measure the performance of the filter), *Naehr and Toffoletto* [2005], as well as others [e.g., *Koller et al.*, 2007; *Shprits et al.*, 2007; *Kondrashov et al.*, 2007] show that the Kalman filter technique accurately reproduces the synthesized electron phase space density (PSD) environment. These studies are generally performed for simplified cases with clearly specified dynamics, but they verify the robustness and functionality of Kalman filters to reproduce 1D radial diffusion.

[9] One such study was performed by *Ni et al.* [2009a], who demonstrated that the Kalman filter is able to reproduce the location and magnitude of PSD peaks and dropouts using two independent data sets. Another example verifying the Kalman filter's practicality was completed by *Daae et al.* [2011], who examined the Kalman filter's robustness to initial conditions, boundary conditions, and loss timescales. This study explicitly demonstrates the Kalman filter technique can reproduce radiation belt dynamics regardless of choice of initial conditions, boundary conditions, or loss timescales. Additionally, they showed that the difference in PSD between drastically different initial conditions is reduced to 15% after one day, and slowly decays to zero on the order of 14 days, quantifying the memory span of the filter. These studies, as well as others [e.g., *Ni et al.*, 2009b], indicate that the Kalman filter is robust to various data, input, and model parameters.

[10] Another data assimilation tool is the observation residual vector, or the innovation vector, which is a measure of the processes that exist in the measurements but are not present in the physical model. *Koller et al.* [2007], *Shprits et al.* [2007], and *Daae et al.* [2011] used the innovation vector to infer enhancements in local acceleration and/or loss. *Shprits et al.* [2012] used the innovation vector to perform a statistical analysis and found a strong correlation between the plasmapause and the location of an inferred source region.

[11] Physical processes can also be estimated directly by including model parameters in the Kalman filter's state vector. This allows for an estimate of, for example, source rate or loss timescale. *Kondrashov et al.* [2007] included loss parameters in the state vector of an EKF. They used an electron PSD data set to estimate the loss timescale inside and outside the plasmasphere for a radial diffusion model with loss. *Reeves et al.* [2012] demonstrated the ability to estimate the time-dependent amplitude parameter of a Gaussian shaped source term for a single storm.

[12] However, until the study presented here, the Kalman filter has not been used to directly estimate source rate location or width, or to estimate the intensity of local heating for more than one storm. In this study, we include a parameterized source rate term in the radial diffusion model and augment the state vector to include source rate parameters. The Kalman filter reconstructs the electron PSD for the full radial range of the outer radiation belt, thereby filling in data gaps in time and space, and estimates the time-dependent intensity of local heating. We perform a parametric study to discern the most likely location and width of the acceleration region for five storm periods. We then use the solutions in a reanalysis of the full 87-day period. The result is a time dependent estimate of the location, extent, and magnitude of local heating. We describe the inputs of the data assimilation scheme in section 2: the data in section 2.1, the model in section 2.2, and the Kalman filter technique in section 2.3. The detailed results of the parametric study and reanalysis are presented in section 3, which are then discussed in section 4.

2. Data Assimilation Inputs and Methodology

2.1. Input: Data

[13] We use energetic electron data from the Synchronous Orbit Particle Analyzer (SOPA) instrument aboard Los Alamos National Laboratory satellites at geosynchronous orbit (LANL-GEO: 97a, 1991–080, 1990–095) [*Belian et al.*,

1992], the Burst Detector Dosimiter (BDD) II aboard a Global Positioning System (GPS) satellite (GPS-ns41) [*Feldman et al.*, 1985], and the Comprehensive Energetic Particle and Pitch Angle Distribution Experiment on Polar (CEP-PAD) [*Blake et al.*, 1995]. The data spans an 87-day period from June 30th to October 24th, 2002. The data are averaged to the center of each discrete mesh grid point with dimensions 0.25[L] × 120[min]. The conversion to PSD and intercalibration [*Friedel et al.*, 2005] is done for constant first and second adiabatic invariants: μ = 2083 (MeV/G) and K = 0.03 ($G^{1/2}R_E$), corresponding to ~1 MeV at GEO. It is performed in two steps: 1) transforming the spacecraft coordinates into phase space coordinates and 2) converting the measured fluxes into PSD values [*Chen et al.*, 2005, 2006]. The electron flux, j(E, α, $\vec{r}$), as a function of energy (E), pitch angle (α), and satellite position ($\vec{r}$), is converted into PSD following *Hilmer et al.* [2000].

2.2. Input: Physical Model

[14] The energetic electron population is often described in phase space coordinates. Phase space corresponds to a six dimensional position-momentum space, but can be reduced to three dimensions by averaging over the three periodic motions: gyration, bounce, and drift. Relativistic electron populations can be described by their PSD: f(μ, K, L, t) [*Schulz and Lanzerotti*, 1974], where μ is the first adiabatic invariant associated with gyration around a field line, K is the second adiabatic invariant associated with particle bounce motion between magnetic mirror points, and L is the Roederer L* parameter [*Roederer*, 1970] related to the third adiabatic invariant ϕ, which is associated with the drift motion of the particle about the Earth. Phase space coordinates are useful because the particle distribution function is constant along a dynamical trajectory in absence of external or internal sources or losses (such as diffusion, wave-particle interactions, etc.), aiding in the identification of system dynamics. When the distribution function is not conserved, phase space coordinates can help identify non-adiabatic heating or loss mechanisms, including location and magnitude.

[15] Radial diffusion in energetic electron populations can be described in PSD coordinates with a Fokker-Plank equation for constant μ and K. We use a one-dimensional Fokker-Plank equation to describe the radial diffusion in L

$$\frac{\partial f}{\partial t} = L^2 \frac{\partial}{\partial L}\left(\frac{D_{LL}}{L^2}\frac{\partial f}{\partial L}\right) - \frac{f}{\tau} + S, \tag{1}$$

where D_{LL}(L, t) is the radial diffusion coefficient, τ(L, t) is the loss timescale, S(L, t) is the source rate, where a three-dimensional model also includes diffusion in pitch angle and energy. We assume a Gaussian form for the source rate, i.e.

$$S = Ae^{-\frac{(L-L_C)^2}{\sigma^2}}, \tag{2}$$

where the source rate is centered at L_C, with width σ and amplitude A. This source function exists over all values in L, and thus does not introduce any artificial discontinuities. Note that we separate source rate and loss terms. The resulting PSD is the net result of the balance between radial transport, source, and loss for particles for only one specific combination of first and second adiabatic invariants, here μ = 2083[MeV/G] and K = 0.03[$G^{1/2}R_E$].

[16] The Crank-Nicolson method [*Crank and Nicolson*, 1947], which is unconditionally stable and 2nd order accurate, is used to solve the equations and does not need to satisfy the Courant condition [*Press et al.*, 1986]. We assume a discrete meshed grid of 32 points from $2 \le L \le 10$. We select a relatively large spatial resolution of L = 0.25 to mitigate radial errors that could occur, for example, in the choice of magnetic field model [*Ni et al.*, 2009b], D_{LL} coefficient [*Brautigam and Albert*, 2000], satellite intercalibration [*Friedel et al.*, 2005] or PSD calculations [*Chen et al.*, 2005]. Our initial condition is a Gaussian fit to an average of the first 20 h of GEO data. On a relevant note, work by *Daae et al.* [2011] show that the initial conditions are 'forgotten' in ~1 day. That is, the filter takes ~1 day to 'spin-up', after which the PSD estimate is nearly identical regardless of the imposed initial condition.

[17] We choose the widely used Kp dependent diffusion coefficient: $D_{LL}(Kp, L) = 10^{(0.506Kp-9.325)}L^{10}$ [*Brautigam and Albert*, 2000], where Kp is an index indicating the magnitude of geomagnetic activity. Since the loss is included separately in the model, we choose three L-dependent loss timescales. To represent plasmaspheric hiss, the loss timescale inside the plasmapause ($L < L_{PP}$) is τ = 8 days [*Kondrashov et al.*, 2007]. For loss mechanisms occurring outside of the plasmapause, but inside the last closed drift shell ($L_{pp} \le L < L_{MAX}$), we choose τ = 3/Kp [*Shprits et al.*, 2005; *Kondrashov et al.*, 2007]. For particles at the last closed drift shell and beyond, we assign a loss timescale of τ = 10 min as these particles will be lost to the magnetopause on the timescale of minutes (approximately 1/2 of a drift period).

[18] We calculate the plasmapause and last closed drift shell using the Dst index, which is an indicator of geomagnetic storm activity. The plasmapause location is assumed to be $L_{PP}(Dst) = -1.57 \log_{10}(\min_{-24,0}Dst) + 6.3$, where the notation $\min_{-24,0}Dst$ represents the minimum Dst value for the past 24 h [*O'Brien and Moldwin*, 2003]. We approximate the last closed drift shell with a second order polynomial fit as described in *Koller and Morley* [2010]. The fitted function is $L_{MAX} = 6.07 \times 10^{-5}Dst^2 + 0.0436Dst + 9.37$, which is derived from the last closed drift shell using the TS03 model [*Tsyganenko et al.*, 2003] during July–December 2002. The PSD at the inner and outer boundaries, L = 2 and L = 10, is set to 1×10^{-16} (c/MeV/cm)^3 based on various studies where, during geomagnetically active times, radial diffusion alone is insufficient to explain PSD peaks near GEO [*Brautigam and Albert*, 2000; *Green and Kivelson*, 2004; *Chen et al.*, 2007].

[19] It is pertinent to recognize that the source rate in our model can have a negative value. In this case, the existing loss in the model is insufficient to match observations, and the filter creates additional loss in the form of negative source. When the source rate term has a positive value, it may indicate an enhancement of an acceleration process or a suppression of loss mechanisms, as the resulting PSD depends on the net contributions of both the loss and source terms, as well as radial diffusion. Actual observational data cannot distinguish between these various processes and measure only the net effect of all the processes in combination. Models, such as the one presented, are a justified attempt to separate and quantify their respective dynamics.

Table 1. Description and Dimension of Vectors, Matrices, and Operators Used in the Kalman Filter[a]

	Description	Dimension
Model Variables		
x_a	Analysis state vector	n × 1
x_f	Forecast state vector	n × 1
$\mathbf{P}_a$	Analysis covariance matrix	n × n
$\mathbf{P}_f$	Forecast covariance matrix	n × n
$\mathbf{Q}$	Model covariance propagating matrix	n × n
$\mathbf{H}$	Observation mapping operator	m × n
$\mathbf{K}$	Kalman gain matrix	n × m
$\mathbf{M}$	Forecast model operator	n × n
Observation Variables		
y	Observation vector	m × 1
$\mathbf{R}$	Observation covariance	m × m

[a]The value n represents the number of values being estimated by the filter and m is the number of observations at a given time t_i.

2.3. The Kalman Filter

[20] The Kalman filter [*Kalman*, 1960] is a sequential data assimilation method that uses weighted least square minimization based on the uncertainties in both the observations, y, and the model state, x. The algorithm is optimized for linear systems for which a Gaussian probability distribution is assumed. The variables used in the Kalman filter, as well as their descriptions and sizes, are outlined in Table 1. The filter consists of two major operations: an analysis step and a forecast step.

[21] The first operation in the analysis step is to calculate the Kalman gain matrix $\mathbf{K}_i$ (equation 3), which is a weighting matrix computed from the model error covariance matrix $\mathbf{P}_i$, and the observational uncertainty $\mathbf{R}_i$. The subscript i represents the time step of operation. The Kalman gain matrix is used to weight the state and observation in subsequent analysis steps, and is defined as

$$\mathbf{K}_i = \mathbf{P}^f(t_i)\mathbf{H}_i^T\left[\mathbf{H}_i\mathbf{P}^f(t_i)\mathbf{H}_i^T + \mathbf{R}_i\right]^{-1}, \tag{3}$$

where $\mathbf{R}_i = \varepsilon_o\mathbf{I} \times y_i$. Here, $\mathbf{H}_i$ is an observation operator that maps the model space into the observational space, the superscript f represents the forecasted state, and ε_o represents the uncertainty of the observations and is set to 30% of the measured PSD [*Koller et al.*, 2007]. $\mathbf{I}$ is the identity matrix.

[22] The analysis state vector x_i^a, and model covariance matrix $\mathbf{P}_i^a$ are given by the Kalman update equations

$$x^a(t_i) = x^f(t_i) + \mathbf{K}_i d_i, \tag{4}$$

$$d_i = y_i^o - \mathbf{H}_i\left[x^f(t_i)\right], \tag{5}$$

$$\mathbf{P}^a(t_i) = (\mathbf{I} - \mathbf{K}_i\mathbf{H}_i)\mathbf{P}^f(t_i), \tag{6}$$

where the superscript a denotes the analysis state after the Kalman update. As can be seen from equation (4), the analysis state vector x_i^a is computed through adjusting the forecasted state vector x_i^f by weighting the difference between the observations and the model forecast with the Kalman gain matrix. In equation (5), d_i is called the observation residual vector or the innovation vector, and the product $\mathbf{K}_i d_i$ is known as the Kalman innovation vector.

[23] The analysis state is then propagated forward in time using the linear forecast model operator $\mathbf{M}_i$, solved by the Crank-Nicolson method [*Crank and Nicolson*, 1947], to create the forecast state:

$$x^f(t_{i+1}) = \mathbf{M}_i[x^a(t_i)] \tag{7}$$

$$\mathbf{P}^f(t_{i+1}) = \mathbf{M}_i\mathbf{P}^a(t_i)\mathbf{M}^T{}_i + \mathbf{Q}(t_i) \tag{8}$$

where $\mathbf{Q}_i = \varepsilon_m\mathbf{I} \times [x_i^f - x_i^a]$ is a diagonal error covariance propagating matrix and represents the decrease in confidence in the model as time evolves away from observation. Its value, $x_t^f - x_t^a$, is a good representation of the performance of the model; that is, a large (small) value indicates poor (good) performance, and thus the model covariance will increase faster (slower). The uncertainty of the model ε_m is a very difficult value to quantify. It is ambiguously set to ten times the observational uncertainty, or ε_m = 300%, since our confidence in our simple one-dimensional model is much lower than observations. This observation error/model error ratio is roughly consistent with previous work [*Shprits et al.*, 2007; *Ni et al.*, 2009a, 2009b; *Daae et al.*, 2011; *Shprits et al.*, 2012]. In a future study, the model uncertainty will be replaced with a dynamic model automatically adjusting the model uncertainty as a function of the innovation vector as described in *Godinez and Koller* [2012].

[24] Whereas most previous radiation belt Kalman filter studies define the state vector to be electron PSD for the full radial range, here we create an augmented system to also include source parameters as additional state variables [e.g., *Lainiotis*, 1971; *Ljung*, 1979]. Since equation (1) is linear in A, we are able to simply append the state vector (x), state error (ε), and forward linear model operator ($\mathbf{M}$) to include this additional parameter for assimilation; that is, we define an augmented state vector, error, and forward model operator as

$$\varepsilon = [\,\varepsilon_{f_1} \quad \varepsilon_{f_2} \quad \cdots \quad \varepsilon_{f_n} \quad \varepsilon_A\,]^T \; x = [f_1 \quad f_2 \quad \cdots \quad f_n \quad A]^T \tag{9}$$

$$M = \begin{bmatrix} \overline{M} & 0 \\ 0 & 1 \end{bmatrix}, \tag{10}$$

where $\varepsilon_{f1} \ldots \varepsilon_{fn,}$ and ε_A correspond to the flux uncertainties at the 1st … nth grid points and the uncertainty in A, respectively.

3. Parametric Study of Source Parameters

[25] The augmented Kalman filter algorithm is only capable of estimating the amplitude parameter of the source term. We must assign values for the location and width parameters. However, these terms are physically dynamic, most likely changing throughout individual storms. To find the most accurate source term location and width for specific periods we employ the observation residual, or the innovation vector, ($y_i - \mathbf{H}_i x_i^f$), which represents the residual between the observations at time i and the model's forecast of the state at time i. It is a measure of the fidelity of the model or, in other words, it is an attempt to quantify physics that are present in the observations but absent from the model.

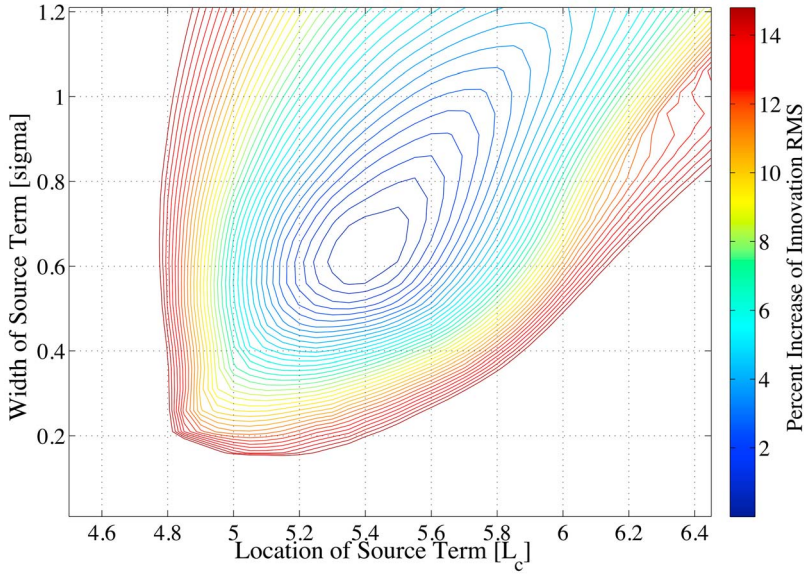

Figure 1. The innovation vector RMS parameter space as a function of the Gaussian source width (y axis) and location (x axis) for July 30th 04:00 to August 21st 00:00. Although the rest of the parameter space is not shown, the minimum depicted is a global minimum.

[26] The RMS of the innovation vector is defined as

$$RMS_{INNOVATION} = \sqrt{\frac{1}{m}\sum_{i=1}^{T}\left(y_i - H_i x_i^f\right)^2} \qquad (11)$$

where T is the total number of time steps over the considered storm period and m is the number of observations. It is a reliable method to quantify the accuracy of the model, by measuring the discrepancy between model forecast and observations. A low (high) innovation vector RMS indicates that the model, including the location and width of the source rate, more (less) accurately predicts the actual measurements. Thus, the lowest innovation vector RMS establishes the solution in location-width parameter that can best reproduce the observed measurements.

[27] Figure 1 represents the innovation vector RMS parameter space for July 30th 04:00 to August 21st 00:00 (which represents storm period 1 - see Table 2). To generate this figure, a series of simulations are performed, each with a discrete pair of source region parameters ranging from L_C = 4.5–6.6 and σ = 0.01–1.6. The innovation RMS is calculated for an individual model run, as each run corresponds to a unique source region. The minimum, located at L_C = 5.4 and σ = 0.6, represents the parameters that best reproduce the observations. These parameters are then applied to the source rate term and used in the reanalysis presented in Figure 2. Figure 2a shows the gridded PSD measurements used. Figure 2b shows the reanalyzed data set with the gaps across space and time filled in, plotted with the real observations. The source rate amplitude parameter A is estimated through the assimilation and plotted as a function of time in Figure 2c. Together with the ascertained location and width, the amplitude parameter completes the prediction of the source rate term and quantifies the location, extent, and magnitude of local heating during this period.

[28] An important note is that the innovation vector RMS is a relatively stable measure of the accuracy of the assimilated results and not sensitive to the variable parameters. That is, small changes in innovation vector RMS are associated with significant changes in source rate parameters. For example, in Figure 1, a 1% change in RMS corresponds to a 0.4 variation in L_C and a 0.35 change in width. However, the innovation RMS for the same period without a source term is 28.9% higher than the same analysis including the source term. In other words, the model performs unquestionably better when the filter is allowed to adjust the amplitude of the source parameter, decidedly justifying its inclusion.

[29] The period of July 30th to October 25th is divided into storm periods, where each storm period begins upon achieving the two criteria: 1) Dst < −80 nT and 2) the first criterion has not been met in the previous four days. Each storm period is assimilated including three days preceding

Table 2. The Individual Storm Periods Outlined With the Location and Width of the Source Term to Minimize the Innovation Vector RMS

Storm Period	Reanalysis Start Date	Storm Criteria Achieved	Reanalysis End Date	L_C	σ
1	July 30th 04:00	Aug. 2nd 04:00	Aug. 21st 00:00	5.4	0.6
2	Aug. 18th 00:00	Aug. 21st 00:00	Sept. 4th 04:00	5.4	1.5
3	Sept. 1st 04:00	Sept. 4th 04:00	Oct. 1st 10:00	6.1	1.3
4	Sept. 28th 10:00	Oct. 1st 10:00	Oct. 14th 13:00	3.9–4.2	Likely <0.6
5	Oct. 11th 13:00	Oct. 14th 13:00	Oct. 24th 00:00	7.1	1.3

the achievement of the criteria to allow sufficient time for the filter to calibrate. The specifics for the resulting five periods are outlined in the first four columns of Table 2. An innovation RMS parametric study is performed for all five storm periods and the results are outlined in the right two columns in Table 2.

[30] Whereas most periods result in a straightforward minimum in location-width space, storm period 4 presents distinctive results. A storm of Dst = −180 nT occurs on October 1st (day of year [DOY] 274), and the resulting PSD peak occurs near L = 4. Intuitively, one would expect that the residual RMS to be smallest for $L_C \approx 4$. Indeed, a source region centered between L = 3.9–4.2 minimizes the innovation RMS. However, because of the proximity of this source region to the plasmapause (which is already compressed to small L), source widths greater than $\sigma \approx 0.6$ considerably populate the slot region. Without measurements below L = 3.5 to locally update the filter, the slot region accumulates PSD from the source term. Although rare, heating near L = 3 is possible during periods of high geomagnetic activity [*Shprits et al.*, 2012]. Thus, without measurements in this region, we cannot specify the width of the source region for this period, although a width of $\sigma < 0.6$ does not allow significant PSD accumulations inside of L = 3.

[31] Since source location and width parameters are specified for each period, reanalysis of the 87-day period is performed with the source parameters changing appropriately for each storm period. The resulting reanalysis is shown in Figure 3. Figure 3b portrays the data from Figure 3a superposed on top of the reanalyzed PSD data set. The spatiotemporal gaps in PSD are filled, allowing for an estimate of electron PSD for the entire radial range of the radiation belt. The full source term, including all three parameters – L_C and σ from the innovation RMS analysis and A directly from the state vector – is pictured in Figure 3c. Figure 3c visualizes the magnitude and extent of local heating occurring during this period. Notice that discontinuities do not occur in the state vector, which allows for a space- and time-continuous estimate for PSD and source rate amplitude, even over boundaries between storm periods. Figure 3d depicts the amplitude term only and quantitatively conveys the intensity of the heating.

[32] The source rate function, which consists of time series estimates of three source rate parameters, is used in a simple one-dimensional diffusion model (equation (1)) without assimilation for comparison. Identical diffusion rates and loss timescales are used, as described in section 2.2. The time series of the local acceleration function (visualized in Figure 3c) is applied in the model. The results are shown in Figure 4a. As expected, the resulting PSD from the 1D diffusion model is very similar to the reanalyzed PSD. We quantify the 1D diffusion model's ability to reproduce the observations in Figure 4b, where the PSD observations (Figure 3a) are directly compared to the results of the simple 1D diffusion model. The diffusion model with no assimilation is able to reproduce the majority of the observations within a factor of 2.

4. Discussion

[33] This study is performed for only a single pair of first and second adiabatic invariants, μ and K, and captures only a small subset of the dynamics of the radiation belts. A reanalysis of all available μ and K combinations is beyond the scope of this study, but will be performed to gain insight on a more comprehensive global picture. The presented analysis demonstrates the pertinence of using data assimilation techniques to do science on the observationally sparse radiation belts, and also allows us to perform science on this particular set of energetic electrons.

[34] Upon closer inspection of the acceleration enhancements in Figure 3, it is apparent that the energization of outer belt electrons generally occurs in the recovery phase of the storms, as expected from elevated ULF wave [e.g., *Elkington et al.*, 1999] and chorus wave activity [e.g., *Li et al.*, 1997; *Bortnik and Thorne*, 2007]. Additionally, the source region occurs inside of GEO for four of the five storm periods analyzed and the widths vary appreciably between σ = 0.6–1.5. The fluctuation in source rate magnitude is significant, changing orders of magnitudes over hours to days, but the timescale could be limited to the resolution of the analysis. The maximum rate of approximately 3.0×10^{-6} $(\mathrm{c/cm/MeV})^3\mathrm{day}^{-1}$ occurs on August 14th at 20:00 (DOY 226), but local maxima are varied for each storm period. This maximum rate, if sustained, is capable of completely repopulating the radiation belt to the largest observed value in ~17 h. The third storm period (August 21st 00:00 to September 4th 04:00 [DOY 233–247]) has the smallest enhancements, the largest of which is 2.1×10^{-7} $(\mathrm{c/cm/MeV})^3\mathrm{day}^{-1}$, which would repopulate the radiation belt in ~10 days, if sustained. The source rates are sufficient to show that local heating is a major factor in populating the electron radiation belts during storm recovery phases. An interesting extension of this work will be to determine the relationship of the source term between multiple combinations of first and second invariant pairs in addition to higher temporal resolution and correlation between solar wind drivers. The temporal evolution between low-energy and high-energy electrons could be examined as per *Turner and Li* [2008b], for example.

[35] We briefly investigate the effect of magnetopause loss timescales by rerunning the simulation with loss timescales two times larger and two times smaller for $L > L_{MAX}$. That is, we perform the same analysis, but with loss timescales above the last closed drift shell equal to τ = 5 min and τ = 20 min (instead of τ = 10 min). The locations and widths of the source terms are reproduced identically for all storm periods except for the 20-min timescale, where for storm period five L_C changes from 7.1 to 6.7 and the width from 1.3 to 1.1, and for storm period three where the width changes from 1.3 to 1.2. The other storm periods are unaffected by either a 5 or 20 min loss timescale above L_{MAX}.

[36] Estimation of source rate location and width is completely novel in data assimilation applications of the electron radiation belts. However, other Kalman filter studies, which also use 1-D models for a single first and second adiabatic invariant pair, have constrained the source region's location and width. The results of our parametric study agree with previous data assimilation in principle. *Shprits et al.* [2007] used a CRRES PSD data set (for less energetic particles of μ = 700[MeV/G] and K = 0.11[$G^{1/2}R_E$]) from August 18th to October 7th, 1990 and averaged the Kalman innovation vector to find missing source region resembling a positively skewed Gaussian centered at L = 5.5 with width $\sigma \approx$ 0.3–0.8.

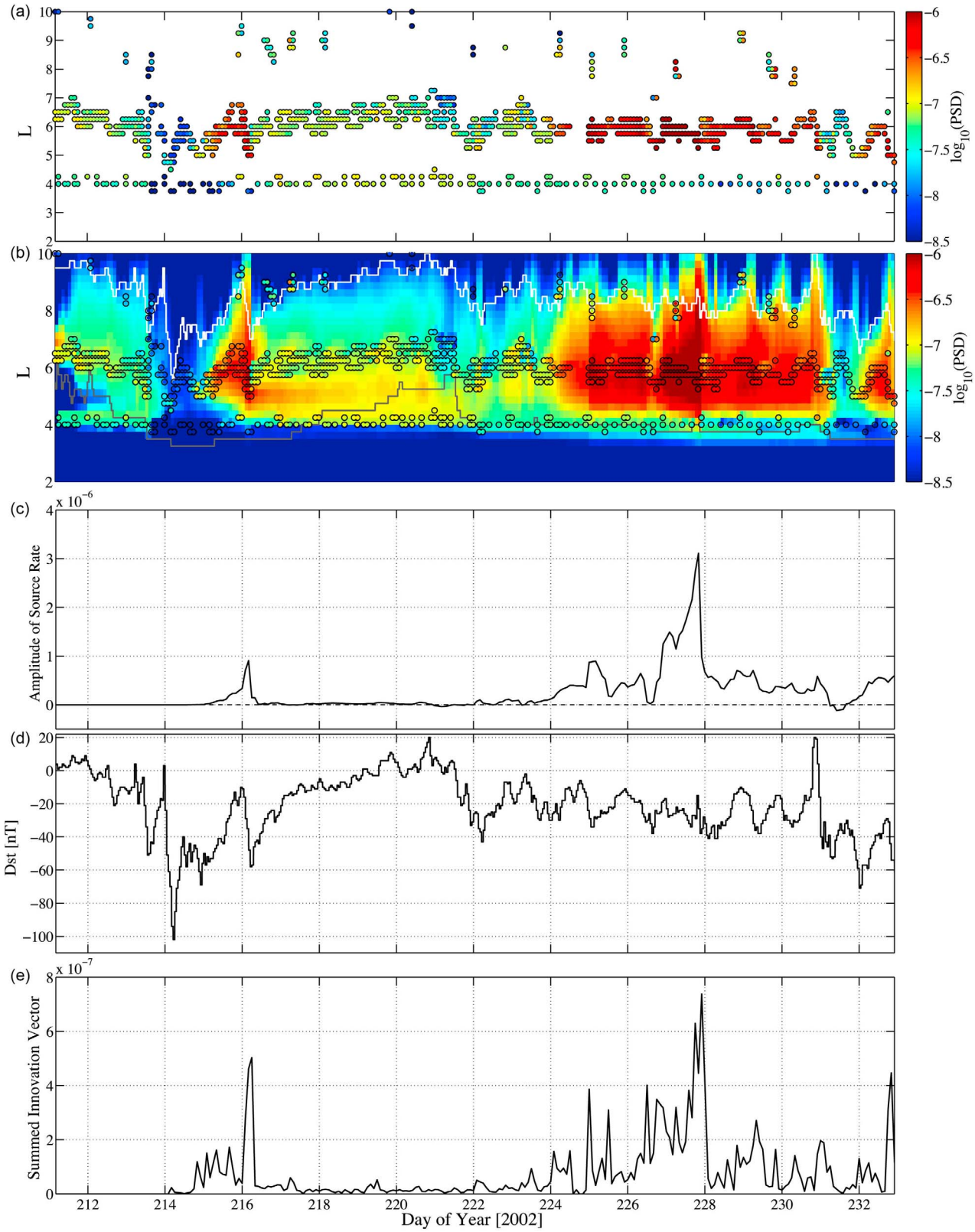

Figure 2. Data reanalysis from July 30th 04:00 to August 21st 00:00 with the source term at $L_C = 5.4$ and width $\sigma = 0.6$. (a) Electron PSD data set used in the assimilation. (b) The reanalyzed PSD data set with the data over-plotted for comparison. The white line represents the last closed drift shell and the gray line represents the plasmapause location. (c) The amplitude parameter of the source rate term. (d) The Dst index. (e) The sum of the innovation vector at each time step, averaged by the number of observations (m).

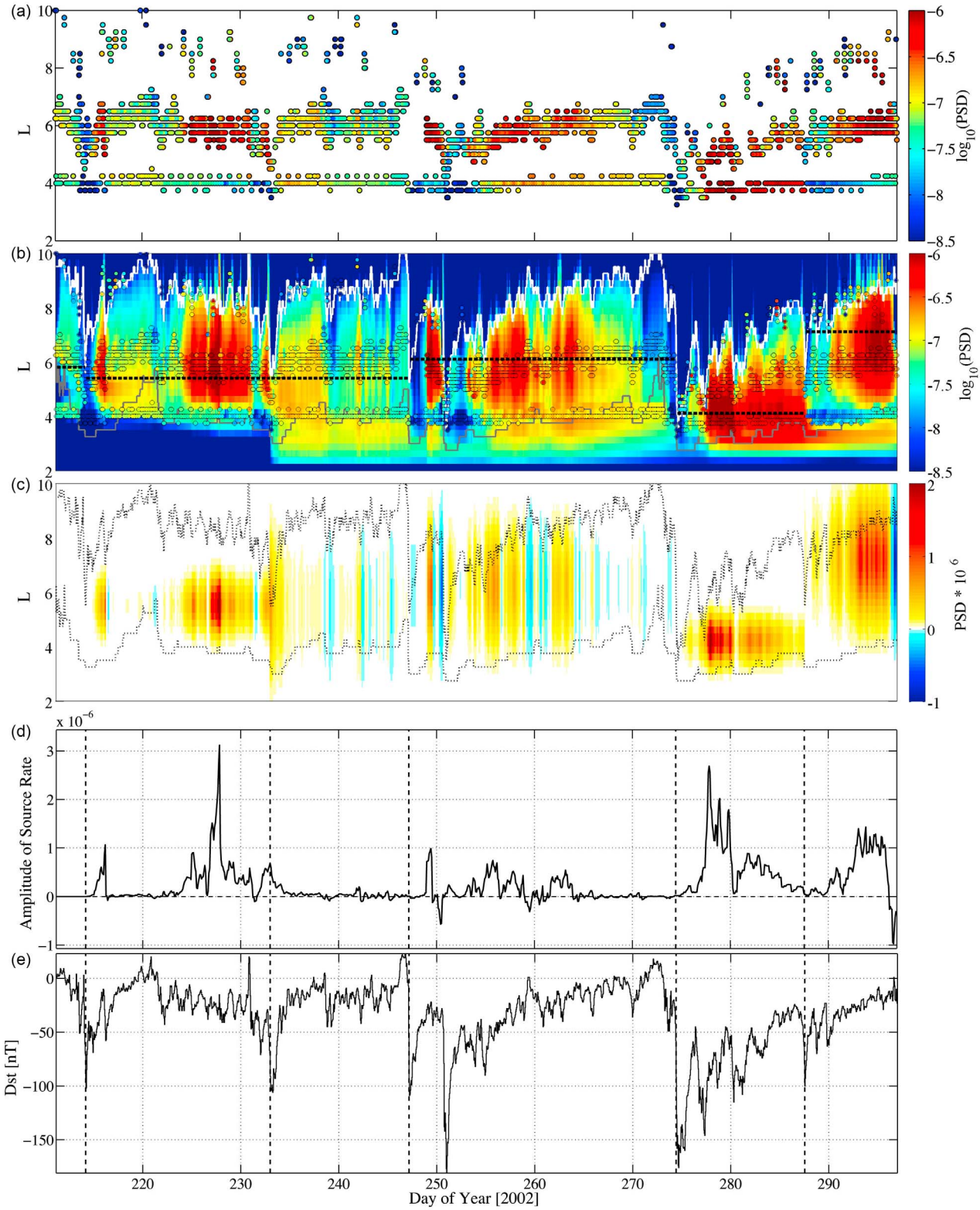

Figure 3. (a) Electron PSD data set used in the assimilation. (b) Reanalyzed PSD with data overlay. The white line corresponds to the last closed drift shell and the gray line to the plasmapause location. (c) The source term, where red/yellow colors represent a positive source term and blue values represent a negative source term. For reference, the upper dotted line represents the last closed drift shell and the lower dotted line represents the plasmapause. (d) The source amplitude parameter. (e) The Dst index. In both Figures 3d and 3e, the vertical dashed lines represent the boundary between consecutive storm periods.

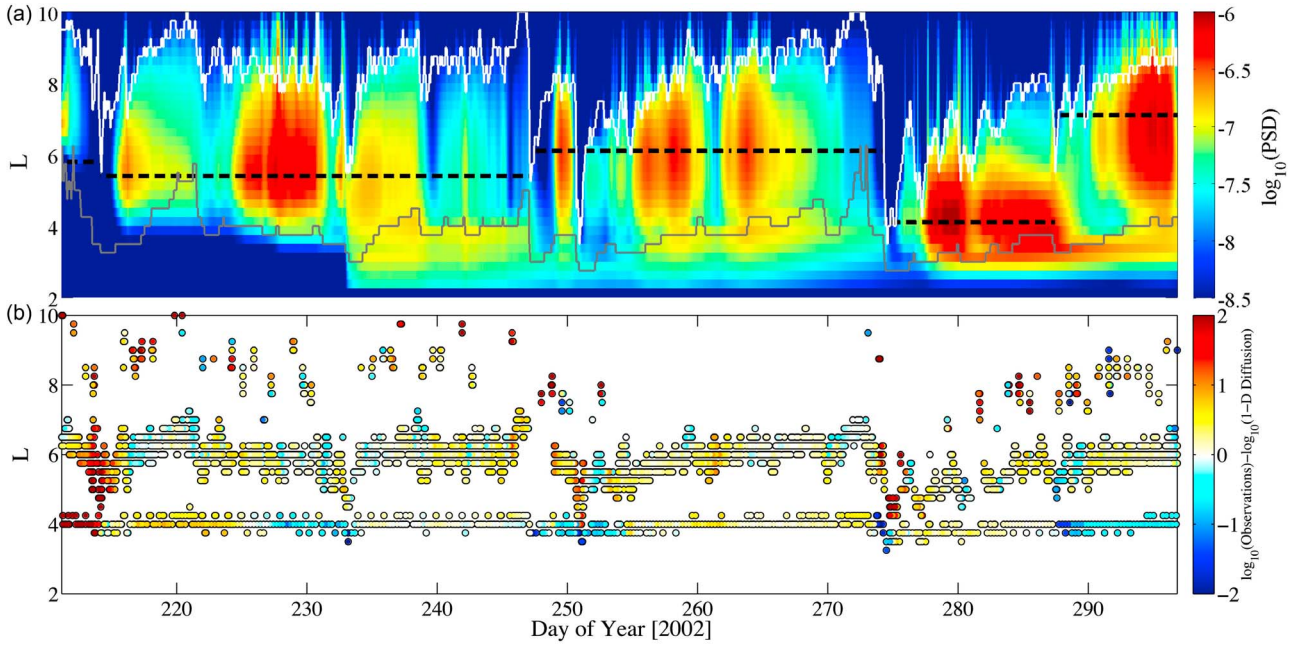

Figure 4. (a) One-dimensional radial diffusion model with no assimilation. The diffusion coefficient and loss terms used are outlined in section 2.2. The full source term from the parametric study is included. (b) The difference between satellite data (Figure 3a) and the radial diffusion model without assimilation.

Daae et al. [2011], using a similar PSD data set (Polar, GPS, and three LANL-GEO for μ = 2083[MeV/G] and K = 0.33[$G^{1/2}R_E$]), inspected the Kalman innovation vector for a variety of different model conditions from June 6th to December 31st, 2002 and repeatedly found evidence of pseudo-Gaussian acceleration occurring between $5 \leq L \leq 6$, with widths between $\sigma \approx 0.6$–0.9. However, both of these studies assimilated multiple storms, so the results are a long-term average of source processes. *Koller et al.* [2007] used a similar PSD data set (Polar, GPS, and three LANL-GEO for μ = 2083[MeV/G] and K = 0.1[$G^{1/2}R_E$]) for the October 24th, 2002 storm (October 25th -November 2nd [DOY 298–306]) and summed the Kalman innovation vector to find a Gaussian-shaped source region close L = 5.5 with width $\sigma \approx 0.3$.

[37] *Reeves et al.* [2012] demonstrated that the Dynamic Radiation Environment Assimilation Model (DREAM) has the capabilities to estimate the amplitude of a Gaussian source region in a comparable method to that presented here. They used a similar data set (Polar, GPS, and three LANL-GEO), for μ = 2083[MeV/G] and K = 0.03[$G^{1/2}R_E$], and an ensemble Kalman filter [*Evensen*, 2003], to provide an amplitude estimate for the same storm period as *Koller et al.* [2007]: October 21st to November 4th, 2002. *Reeves et al.* [2012] chose the source location and width to compensate for the dual-peak nature of the reanalyzed PSD, which is caused by observations at GEO and GPS with extensive data gaps in the region L $\sim$ 4–6. Hence, they choose a source location of L = 5 with width of σ = 1, which eliminates the PSD trough between GEO and GPS observations. The intensity of local heating peaks in the pre-storm phase, which is an artifact of the filter using the source term to compensate for the dual-peaked initial condition. They find, as presented in this study, that the source rate intensifies in the recovery phase.

[38] Our findings agree with results from non-assimilative studies that find peaks in electron PSD below GEO. Modeling done with the 3-D VERB diffusion code [*Shprits et al.*, 2008], including chorus wave interactions, found peaks in PSD at L $\sim$ 4–6 for electrons with μ = 700 MeV/G. Similarly, modeling done with the 3-D Salammbo code [*Beutier and Boscher*, 1995], including interactions with chorus waves, found PSD peaks for 3100 MeV/G electrons near L = 5.5 during the recovery phase [*Varotsou et al.*, 2005]. These physics-based models are consistent with our findings.

[39] Investigations of electron PSD radial gradients using LANL-GEO data conclude localized acceleration occurring inside of GEO for electrons with μ = 2000[MeV/G] [*Turner and Li*, 2008a; *Turner et al.*, 2010] and for electrons with 1.1–1.5 MeV [*Shi et al.*, 2009]. More comprehensively, *Green and Kivelson* [2004] (for electrons with μ = 2000[MeV/G] and K > 500[$G^{1/2}R_E$]) and *Chen et al.* [2006] (for electrons with μ = 2083[MeV/G] and K = 0.1[$G^{1/2}R_E$]) were able to estimate local heating occurring near L = 5 and L = 5–6, respectively. Additionally, *O'Brien et al.* [2003] found associations between acceleration and VLF/ELF chorus waves occurring near L $\sim$ 5 for electrons of 1.8–3.5 MeV and >1.5 MeV. These studies, which arrive at similar conclusion for a variety of μ and K pairs, but in different ways, reinforce the theory of internal acceleration mechanisms occurring near GEO.

5. Summary

[40] We use a Kalman filter, which blends energetic electron measurements of a specific pair of first and second adiabatic invariants with a one dimensional radial diffusion model, to produce an estimate of the outer radiation belt environment that is more accurate than either independently. Although the in situ energetic electron measurements are

sparse, the Kalman filter technique is capable of filling in spatiotemporal data gaps for constant μ and K and has proven robust for this application [e.g., *Naehr and Toffoletto*, 2005; *Ni et al.*, 2009a, 2009b; *Daae et al.*, 2011]. Previously, PSD values, loss timescales, and source rate have been determined using a Kalman filter, but this is the first attempt to quantitatively estimate source location and width, as well as the source rate over multiple storms. Specifically, we calculate the location and extent of the heating regions and quantify the time-dependent intensity of the enhancements.

[41] Electron phase space density (PSD) observations from five satellites (three LANL geosynchronous, a GPS, and Polar) for μ = 2083[MeV/G] and K = 0.03[$G^{1/2}R_E$] are combined with a one-dimensional radial diffusion model that includes loss and parameterized local acceleration. The state vector is augmented to include an estimable amplitude parameter for a Gaussian source rate term; thus, we are able to estimate the rate of local heating as a function of time. Other source term parameters include location and width, which are assigned values for each simulated period and are not directly estimated by the filter. However, we are able to estimate them using a parametric study, in which we use the innovation vector to find the most accurate solution in location-width parameter space. The innovation vector is a tool that measures of the performance of the model with respect to actual observations, and is used to quantify physics that are present in the observations but absent in the model.

[42] The analysis period, July 30th to October 24th, is divided into five storm periods (based on Dst criteria), and for each period the root mean square (RMS) of the innovation vector is calculated for various locations and widths. The RMS minimum indicates source rate parameters that best match the observations, consequently defining the most likely location and width of the source region. A detailed analysis of July 30th 04:00 to August 21st 00:00 (DOY 211 to 233), 2002, is presented as an example. We find that the minimum innovation vector RMS for this period occurs with source occurring at L = 5.4 with width σ = 0.6. The analysis is performed for all five periods and the results are included in a reanalysis of the full 87-day period. The resulting assimilated data consists of constant μ and K PSD for the full radial range, with spatial and temporal observational gaps filled, and an estimate of the source rate amplitude parameter as a function of time.

[43] The source regions are found to occur within GEO for four of the five periods analyzed. Furthermore, close inspection of its intensity shows orders-of-magnitude fluctuations on the timescales of hours. The magnitude of the enhancements increases during the recovery phase of many of the storms, consistent with occurrences of ULF and chorus wave activity [e.g., *Li et al.*, 1997; *Elkington et al.*, 1999; *Bortnik and Thorne*, 2007]. Additionally, local peaks of the acceleration enhancements are almost exclusively found during the recovery phase. The magnitude of the enhancements indicates that local heating is a significant contributor to the energetic electron population. In fact, the rate shows that local heating is capable of completely repopulating the radiation belt after a full dropout.

[44] The presented Kalman filter results are consistent with past data assimilation studies and previous PSD gradient studies, and confirm the importance of local electron heating near GEO in repopulating the outer radiation belt during the recovery phase of geomagnetic storms. Furthermore, this novel technique advances the applications of Kalman filters to Earth's energetic electron environment and provides a unique perspective on the dynamics of the outer radiation belt.

[45] **Acknowledgments.** This work was supported by NSF grants (CISM, ATM - 0842388, - 0902813, and - 1131869) and also by grant from the National Natural Science Foundation of China (40921063). The authors would like to thank Weichao Tu and Lauren Blum for helpful discussions.

[46] Masaki Fujimoto thanks the reviewers for their assistance in evaluating this paper.

References

Baker, D. N. (2001), Satellite anomalies due to space storms, in *Space Storms and Space Weather Hazards*, edited by I. A. Daglis, pp. 285–311, Springer, New York.

Belian, R. D., G. R. Gisler, T. Cayton, and R. Christensen (1992), High Z energetic particles at geosynchronous orbit during the great solar proton event of October, 1989, *J. Geophys. Res.*, *97*, 16,897–16,906, doi:10.1029/92JA01139.

Beutier, T., and D. Boscher (1995), A three-dimensional analysis of the electron radiation belt by the Salammbô code, *J. Geophys. Res.*, *100*, 14,853–14,861, doi:10.1029/94JA03066.

Blake, J. B., et al. (1995), Comprehensive energetic particle and pitch angle distribution experiment on polar, *Space Sci. Rev.*, *71*, 531–562, doi:10.1007/BF00751340.

Bortnik, J., and R. M. Thorne (2007), The dual role of ELF/VLF chorus waves in the acceleration and precipitation of radiation belt electrons, *J. Atmos. Sol. Terr. Phys.*, *69*, 378–386, doi:10.1016/j.jastp.2006.05.030.

Bourdarie, S., R. H. W. Friedel, J. Fennell, S. Kanekal, and T. E. Cayton (2005), Radiation belt representation of the energetic electron environment: Model and data synthesis using the Salammbô radiation belt transport code and Los Alamos geosynchronous and GPS energetic particle data, *Space Weather*, *3*, S04S01, doi:10.1029/2004SW000065.

Bourdarie, S., A. Sicard-Piet, R. H. W. Friedel, T. P. O'Brien, T. Cayton, B. Blake, D. Boscher, and D. Lazaro (2009), Outer electron belt specification model, *IEEE Trans. Nucl. Sci.*, *56*(4), 2251–2257, doi:10.1109/TNS.2009.2014844.

Brautigam, D. H., and J. M. Albert (2000), Radial diffusion analysis of outer radiation belt electrons during the October 9, 1990, magnetic storm, *J. Geophys. Res.*, *105*, 291–310, doi:10.1029/1999JA900344.

Chen, Y., R. H. W. Friedel, G. D. Reeves, T. G. Onsager, and M. F. Thomsen (2005), Multisatellite determination of the relativistic electron phase space density at geosynchronous orbit: Methodology and results during geomagnetically quiet times, *J. Geophys. Res.*, *110*, A10210, doi:10.1029/2004JA010895.

Chen, Y., R. H. W. Friedel, and G. D. Reeves (2006), Phase space density distributions of energetic electrons in the outer radiation belt during two Geospace Environment Modeling Inner Magnetosphere/Storms selected storms, *J. Geophys. Res.*, *111*, A11S04, doi:10.1029/2006JA011703.

Chen, Y., G. D. Reeves, and R. H. W. Freidel (2007), The energization of relativistic electrons in the outer Van Allen radiation belt, *Nat. Phys.*, *3*, 614–617, doi:10.1038/nphys655.

Crank, J., and P. Nicolson (1947), A practical method for numerical evaluation of solutions of partial differential equations of the heat-conduction type, *Math. Proc. Cambridge Philos. Soc.*, *43*, 50–67, doi:10.1017/S0305004100023197.

Daae, M., Y. Y. Shprits, B. Ni, J. Koller, D. Kondrashov, and Y. Chen (2011), Reanalysis of radiation belt electron phase space density using various boundary conditions and loss model, *Adv. Space Res.*, *48*, 1327–1334, doi:10.1016/j.asr.2011.07.001.

Elkington, S. R., M. K. Hudson, and A. A. Chan (1999), Acceleration of relativistic electrons via drift resonant interactions with toroidal-mode Pc-5 ULF oscillations, *Geophys. Res. Lett.*, *26*, 3273–3276, doi:10.1029/1999GL003659.

Evensen, G. (1994), Sequential data assimilation with a nonlinear quasi-geostrophic model using Monte Carlo methods to forecast error statistics, *J. Geophys. Res.*, *99*(C5), 10,143–10,162, doi:10.1029/94JC00572.

Evensen, G. (2003), The ensemble Kalman filter: Theoretical formulation and practical implementation, *Ocean Dyn.*, *53*, 343–367, doi:10.1007/s10236-003-0036-9.

Feldman, W., Aiello, W., Drake, D., and M. Herrin (1985), The bdd II: An improved electron dosimeter for the Global Positioning System, *LANL Tech. Rep. LA-10453-MS*, Los Alamos Natl. Lab., Los Alamos, N. M.

Friedel, R., Bourdarie, S., and T. E. Cayton (2005), Intercalibration of magnetospheric energetic electron data, *Space Weather*, *3*, S09B04, doi:10.1029/2005SW000153.

Godinez, H. C., and J. Koller (2012), Localized adaptive inflation in ensemble data assimilation for a radiation belt model, *Space Weather*, *10*, S08001, doi:10.1029/2012SW000767.

Green, J. C., and M. G. Kivelson (2004), Relativistic electrons in the outer radiation belt: Differentiating between acceleration mechanisms, *J. Geophys. Res.*, *109*, A03213, doi:10.1029/2003JA010153.

Hilmer, R., G. Ginet, and T. Cayton (2000), Enhancement of equatorial energetic electron fluxes near L = 4.2 as a result of high speed solar wind streams, *J. Geophys. Res.*, *105*, 23,311–23,322, doi:10.1029/1999JA000380.

Horne, R. B., R. M. Thorne, S. A. Glauert, N. P. Meredith, D. Pokhotelov, and O. Santolík (2007), Electron acceleration in the Van Allen radiation belts by fast magnetosonic waves, *Geophys. Res. Lett.*, *34*, L17107, doi:10.1029/2007GL030267.

Jazwinski, A. (1970), *Stochastic Processes and Filtering Theory*, Academic, New York.

Kalman, R. E. (1960), A new approach to linear filtering and prediction problems, *J. Basic Eng.*, *82*, 35–45, doi:10.1115/1.3662552.

Kalnay, E. (2003), *Atmospheric Modeling, Data Assimilation and Predictability*, Cambridge Univ. Press, Cambridge, U. K.

Koller, J., and S. K. Morley (2010), Magnetopause shadowing effects for radiation belt models during high-speed solar wind streams, Abstract SM13A-1787 presented at 2010 Fall Meeting, AGU, San Francisco, Calif., 13–17 Dec.

Koller, J., Y. Chen, G. D. Reeves, R. Friedel, T. E. Cayton, and J. A. Vrugt (2007), Identifying the radiation belt source region by data assimilation, *J. Geophys. Res.*, *112*, A06244, doi:10.1029/2006JA012196.

Kondrashov, D., Y. Shprits, M. Ghil, and R. Thorne (2007), A Kalman filter technique to estimate relativistic electron lifetimes in the outer radiation belt, *J. Geophys. Res.*, *112*, A10227, doi:10.1029/2007JA012583.

Lainiotis, D. G. (1971), Optimal adaptive estimation: Structure and parameter adaptation, *IEEE Trans. Autom. Control*, *16*(2), 160–170, doi:10.1109/TAC.1971.1099684.

Li, W., R. M. Thorne, V. Angelopoulos, J. Bortnik, C. M. Cully, B. Ni, O. LeContel, A. Roux, U. Auster, and W. Magnes (2009), Global distribution of whistler-mode chorus waves observed on the THEMIS spacecraft, *Geophys. Res. Lett.*, *36*, L09104, doi:10.1029/2009GL037595.

Li, X., and M. A. Temerin (2001), The electron radiation belt, *Space Sci. Rev.*, *95*, 569–580, doi:10.1023/A:1005221108016.

Li, X., D. N. Baker, M. Temerin, T. E. Cayton, G. D. Reeves, R. A. Christiansen, J. B. Blake, M. D. Looper, R. Nakamura, and S. G. Kanekal (1997), Multisatellite observations of the outer zone electron variation during the November 3–4, 1993, magnetic storm, *J. Geophys. Res.*, *102*, 14,123–14,140, doi:10.1029/97JA01101.

Ljung, L. (1979), Asymptotic behavior of the extended Kalman filter as a parameter estimator for linear systems, *IEEE Trans. Autom. Control*, *24*(1), 36–50, doi:10.1109/TAC.1979.1101943.

Maget, V., S. Bourdarie, D. Boscher, and R. H. W. Friedel (2007), Data assimilation of LANL satellite data into the Salammbô electron code over a complete solar cycle by direct insertion, *Space Weather*, *5*, S10003, doi:10.1029/2007SW000322.

Meredith, N. P., R. B. Horne, R. H. A. Iles, R. M. Thorne, D. Heynderickx, and R. R. Anderson (2002), Outer zone relativistic electron acceleration associated with substorm-enhanced whistler mode chorus, *J. Geophys. Res.*, *107*(A7), 1144, doi:10.1029/2001JA900146.

Meredith, N. P., M. Cain, R. B. Horne, R. M. Thorne, D. Summers, and R. R. Anderson (2003a), Evidence for chorus-driven electron acceleration to relativistic energies from a survey of geomagnetically disturbed periods, *J. Geophys. Res.*, *108*(A6), 1248, doi:10.1029/2002JA009764.

Meredith, N. P., R. B. Horne, R. M. Thorne, and R. R. Anderson (2003b), Favored regions for chorus-driven electron acceleration to relativistic energies in the Earth's outer radiation belt, *Geophys. Res. Lett.*, *30*(16), 1871, doi:10.1029/2003GL017698.

Naehr, S. M., and F. R. Toffoletto (2005), Radiation belt data assimilation with an extended Kalman filter, *Space Weather*, *3*, S06001, doi:10.1029/2004SW000121.

Ni, B., Y. Shprits, T. Nagai, R. Thorne, Y. Chen, D. Kondrashov, and H.-J. Kim (2009a), Reanalyses of the radiation belt electron phase space density using nearly equatorial CRRES and polar-orbiting Akebono satellite observations, *J. Geophys. Res.*, *114*, A05208, doi:10.1029/2008JA013933.

Ni, B., Y. Shprits, R. Thorne, R. Friedel, and T. Nagai (2009b), Reanalysis of relativistic radiation belt electron phase space density using multisatellite observations: Sensitivity to empirical magnetic field models, *J. Geophys. Res.*, *114*, A12208, doi:10.1029/2009JA014438.

O'Brien, T. P., and M. B. Moldwin (2003), Empirical plasmapause models from magnetic indices, *Geophys. Res. Lett.*, *30*(4), 1152, doi:10.1029/2002GL016007.

O'Brien, T. P., K. R. Lorentzen, I. R. Mann, N. P. Meredith, J. B. Blake, J. F. Fennell, M. D. Looper, D. K. Milling, and R. R. Anderson (2003), Energization of relativistic electrons in the presence of ULF power and MeV microbursts: Evidence for dual ULF and VLF acceleration, *J. Geophys. Res.*, *108*(A8), 1329, doi:10.1029/2002JA009784.

Press, W. H., B. P. Flannery, S. A. Teukolsky, and W. T. Vetterling (1986), *Numerical Recipes—The Art of Scientific Computing*, 1st ed., Cambridge Univ. Press, New York.

Reeves, G. D., K. L. McAdams, R. H. W. Friedel, and T. P. O'Brien (2003), Acceleration and loss of relativistic electrons during geomagnetic storms, *Geophys. Res. Lett.*, *30*(10), 1529, doi:10.1029/2002GL016513.

Reeves, G. D., Y. Chen, G. S. Cunningham, R. W. H. Friedel, M. G. Henderson, V. K. Jordanova, J. Koller, S. K. Morley, M. F. Thomsen, and S. Zaharia (2012), Dynamic Radiation Environment Assimilation Model: DREAM, *Space Weather*, *10*, S03006, doi:10.1029/2011SW000729.

Roederer, J. G. (1970), *Dynamics of Geomagnetically Trapped Radiation*, Springer, New York, doi:10.1007/978-3-642-49300-3.

Santolík, O., D. A. Gurnett, J. S. Pickett, M. Parrot, and N. Cornilleau-Wehrlin (2005), Central position of the source region of storm-time chorus, *Planet. Space Sci.*, *53*, 299–305, doi:10.1016/j.pss.2004.09.056.

Santolík, O., D. A. Gurnett, J. S. Pickett, J. Chum, and N. Cornilleau-Wehrlin (2009), Oblique propagation of whistler mode waves in the chorus source region, *J. Geophys. Res.*, *114*, A00F03, doi:10.1029/2009JA014586.

Schulz, M., and L. J. Lanzerotti (1974), *Particle Diffusion in the Radiation Belts*, Springer, New York, doi:10.1007/978-3-642-65675-0.

Shi, Y., E. Zesta, and L. R. Lyons (2009), Features of energetic particle radial profiles inferred from geosynchronous responses to solar wind dynamic pressure enhancements, *Ann. Geophys.*, *27*, 851–859, doi:10.5194/angeo-27-851-2009.

Shprits, Y. Y., R. M. Thorne, G. D. Reeves, and R. Friedel (2005), Radial diffusion modeling with empirical lifetimes: Comparison with CRRES observations, *Ann. Geophys.*, *23*, 1467–1471, doi:10.5194/angeo-23-1467-2005.

Shprits, Y. Y., R. M. Thorne, R. B. Horne, S. A. Glauert, M. Cartwright, C. T. Russell, D. N. Baker, and S. G. Kanekal (2006), Acceleration mechanism responsible for the formation of the new radiation belt during the 2003 Halloween solar storm, *Geophys. Res. Lett.*, *33*, L05104, doi:10.1029/2005GL024256.

Shprits, Y. Y., D. Kondrashov, Y. Chen, R. Thorne, M. Ghil, R. Friedel, and G. Reeves (2007), Reanalysis of relativistic radiation belt electron fluxes using CRRES satellite data, a radial diffusion model, and a Kalman filter, *J. Geophys. Res.*, *112*, A12216, doi:10.1029/2007JA012579.

Shprits, Y. Y., S. R. Elkington, N. P. Meredith, and D. A. Subbotin (2008), Review of modeling of loss and sources of relativistic electrons in the outer radiation belt I: Radial transport, *J. Atmos. Sol. Terr. Phys.*, *70*, 1679–1693, doi:10.1016/j/jastp.2008.06014.

Shprits, Y., M. Daae, and B. Ni (2012), Statistical analysis of phase space density buildups and dropouts, *J. Geophys. Res.*, *117*, A01219, doi:10.1029/2011JA016939.

Stachura, M., and E. W. Frew (2011), Cooperative target localization with a communication aware unmanned aircraft system, *J. Guid. Control Dyn.*, *34*(5), 1352–1363, doi:10.2514/1.51591.

Summers, D., B. Ni, and N. P. Meredith (2007), Timescales for radiation belt electron acceleration and loss due to resonant wave-particle interactions: 2. Evaluation for VLF chorus, ELF hiss, and electromagnetic ion cyclotron waves, *J. Geophys. Res.*, *112*, A04207, doi:10.1029/2006JA011993.

Tapley, B. D., B. E. Schutz, and G. H. Born (2004), *Statistical Orbit Determination*, Elsevier Academic, Amsterdam.

Tsyganenko, N. A., H. J. Singer, and J. C. Kasper (2003), Storm-time distortion of the inner magnetosphere: How severe can it get?, *J. Geophys. Res.*, *108*(A5), 1209, doi:10.1029/2002JA009808.

Turner, D. L., and X. Li (2008a), Radial gradients of phase space density of the outer radiation belt electrons prior to sudden solar wind pressure enhancements, *Geophys. Res. Lett.*, *35*, L18101, doi:10.1029/2008GL034866.

Turner, D. L., and X. Li (2008b), Quantitative forecast of relativistic electron flux at geosynchronous orbit based on low-energy electron flux, *Space Weather*, *6*, S05005, doi:10.1029/2007SW000354.

Turner, D. L., X. Li, G. D. Reeves, and H. J. Singer (2010), On phase space density radial gradients of Earth's outer-belt electrons prior to sudden solar wind pressure enhancements: Results from distinctive events and a superposed epoch analysis, *J. Geophys. Res.*, *115*, A01205, doi:10.1029/2009JA014423.

Varotsou, A., D. Boscher, S. Bourdarie, R. B. Horne, S. A. Glauert, and N. P. Meredith (2005), Simulation of the outer radiation belt electrons near geosynchronous orbit including both radial diffusion and resonant interaction with Whistler-mode chorus waves, *Geophys. Res. Lett.*, *32*, L19106, doi:10.1029/2005GL023282.